The rapid infilling of a tide-dominated channel on the southern Yangtze Delta plain during the Medieval Climate Anomaly

Zhuoxuan Wu[1], Jianwen Wang[2], Xiaomei Nian[1]*,
Fengyue Qiu[1] and Zhanghua Wang[1,3]*

[1]State Key Laboratory of Estuarine and Coastal Research, East China Normal University,
Shanghai, China, [2]Department of Archaeology, Shanghai Museum, Shanghai, China, [3]Southern Marine
Science and Engineering Guangdong Laboratory, Zhuhai, China

The response of ports and navigation channels in tide-dominated or tide-influenced estuaries to climate warming is of significant practical relevance. However, studies utilizing sedimentary records to understand these dynamics remain limited. This study investigates the rapid siltation of the palaeo-Qinglong channel during the Song dynasty and its relationship to climate change. Three cores were drilled in the lower reaches of the palaeo-Wusong River, and surface sediment samples were collected from the Huangpu River in the southern plain of the Yangtze Delta. Using AMS ^{14}C and optically stimulated luminescence (OSL) dating, sedimentological and alkaline earth metal analyses, this study explores the formation and silting history of the palaeo-Qinglong channel. The results indicate that the palaeo-channel was formed about 2,000 years ago as a fluvial-dominated channel but transitioned into a tide-dominated environment, as evidenced by the prevalence of muddy sediments. Rapid siltation occurred during the 11th and 12th centuries, characterized by increased Sr content and Sr/Ba ratio, which indicate intensified salinity intrusion. This rapid infilling is attributed to the increased storm frequency during the Song dynasty, which enhanced the mud import into the channel. A brief period of strengthened fluvial processes, characterized by the occurrence of sandy bedload in the sediments near Qinglong Town, likely reflects channel regulation projects undertaken along the lower reaches of the palaeo-Wusong River during the Northern Song dynasty. The findings suggest that the climate warming and relative sea-level rise during the Medieval Climate Anomaly (MCA) amplified tidal processes in the lower palaeo-Wusong River. This study provides valuable insights into fluvial-marine interactions and their implications for managing ports and navigation channels in tidally influenced estuaries.

1 Introduction

According to the latest IPCC report, human activities have unequivocally triggered a global climate crisis, resulting in a continuous rise in average surface temperatures (IPCC, 2022). The global average sea levels have risen by ~210 mm since the late 19th century (Church and White, 2011; Hay et al., 2015). As the climate warms and sea levels continue to rise, low-lying coastal regions face increasing challenges, including saltwater intrusion, intensified storm surges, and coastal erosion (Williams, 2013; Cai and Tan, 2020). Understanding how coastal zones have responded to past climate changes is crucial for predicting future fates. In this context, sediments provide essential records for reconstructing environmental responses in the past (Plater et al., 1999; Wu et al., 2022). However, while researches have largely focused on coastal flooding and erosion, the impacts on ports and navigation channels in river mouths, remain underexplored.

In the southern plain of the tide-dominated Yangtze Delta, the Wusong River is a critical waterway linking the Taihu drainage basin with the Yangtze River (Figure 1). Historically, the River functioned as the primary drainage channel for Lake Taihu and featured a notably width (Wei, 1979). Its distributary—the palaeo-Qinglong channel—supported the ancient Port Qinglong, a key hub of foreign trade in the Yangtze Delta during the Song dynasty (Qiao, 1980; Zou, 2007; Wang, 2016; Zhang, 2019). Historical records indicate that siltation in the lower reaches of the palaeo-Wusong
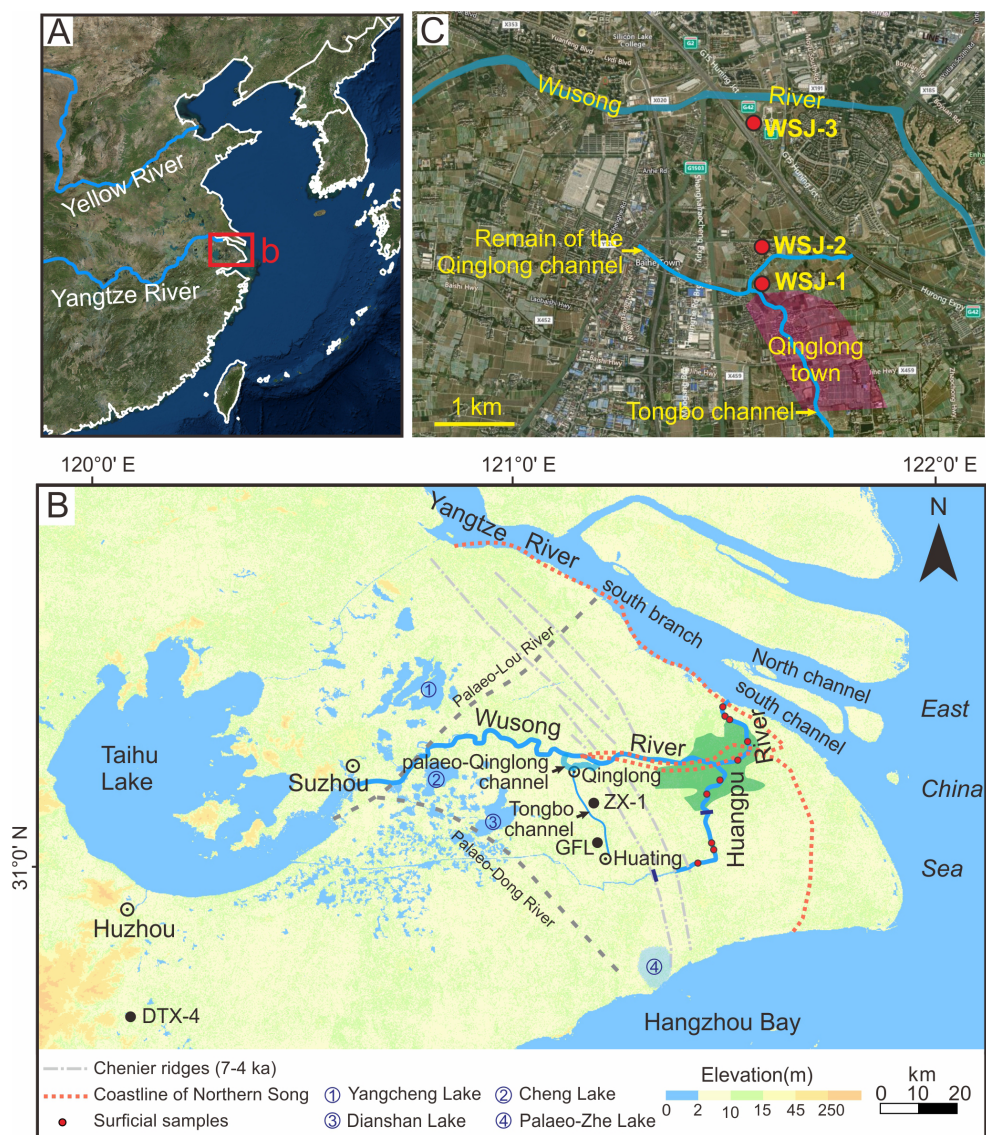
FIGURE 1
Study area and sampling locations. **(A)** Location of the southern Yangtze Delta plain. **(B)** The present-day Wusong and Huangpu rivers, as well as the palaeo-Qinglong channel on the delta plain. The urbanized region of Shanghai is highlighted in green. Also indicated are the locations of surficial samples from the Huangpu River and previously studied cores ZX-1 (Wang et al., 2012), GFL (Wang et al., 2012), and DTX-4 (Chen et al., 2018). The upper, middle and lower reaches of the Huangpu River are marked by dark blue short lines. Note that the South Branch and North Channel of the Yangtze River mouth are fluvial-dominated and tide-influenced, while the South Channel is tide-dominated. **(C)** Locations of sediment cores collected in this study. The inferred area of Qinglong Town is based on archaeological investigations.

River began as early as the Tang dynasty and accelerated during the Song dynasty, leading to the decline of the Port Qinglong (Zhu, 1980b). Similar rapid infilling of distributary channels has been reported in other tide-dominated systems, such as the Mekong Delta (Gugliotta et al., 2021, 2022). However, the sediment dynamics driving such siltation remain insufficiently explored. It is therefore our interest to investigate the fluvial-marine interactions and their role on the channel evolution in the tide-dominated river mouths by focusing on the rapid infilling of the lower palaeo-Wusong River during the Song dynasty.

The Song dynasty (960–1279 CE; 990–671 cal. yr BP) coincides with the Medieval Climate Anomaly (MCA), a well-documented centennial-scale warming phase (Lamb, 1965; Hughes and Diaz, 1994; Crowley and Lowery, 2000; Bradley et al., 2003; Ge et al., 2013). Historical studies suggest that eastern China experienced warmer temperatures during this period, along with relative sea-level rise and an increased frequency of storm tides (Zhu, 1973; Man, 1988; Ni and Ji, 1997; Shi et al., 2009; Man and Yang, 2014; Sun, 2021; Jing, 2023). This research leverages stratigraphic records from the palaeo-lower Wusong River to uncover the mechanisms for the siltation of the Port Qinglong. The findings aim to provide insights for managing port and navigation channel resources in tidally influenced or dominated regions, as well as contribute to basic research on the climate-driven evolution of tidal estuaries.

2 Study area

The Wusong River, historically known as the Songjiang or Songling River, is referred to as the Suzhou River in its Shanghai section. It originates from Taihu Lake and once directly discharged into the Yangtze River mouth, but became a tributary of the Huangpu River in the Ming dynasty because of the siltation in the lower reaches (Figure 1B; Zhu, 1980a). Currently, it spans 125 km with an average width of 40–50 m, a gentle riverbed gradient of only 0.085‰ in the middle and lower reaches, and an average runoff of 10 m³/s (Xu, 1997).

Historically, the Wusong River, along with the palaeo-Loujiang and palaeo-Dongjiang Rivers, formed the primary drainage system of Taihu Lake (Figure 1B). Approximately 3,000 years ago, the river's mouth was located to the east of chenier ridges. Over the past 2,000 years, increased sediment load from the Yangtze River has driven rapid coastline advancement. Between the 5th and 12th centuries, the coastline moved eastward by about 30 km (Figure 1B; Fu, 1998; Zhang, 2006). Factors such as increased sediment deposition, land subsidence, and relative sea-level rise were suggested to have contributed to the narrowing and silting of the rivers' lower reaches. By the Northern Song dynasty, the Wusong River had become the only significant drainage channel for Taihu Lake (Jing, 1985; Hong, 1991). Its mouth also progressively narrowed, shrinking from about 10 km wide during the Tang dynasty (7th–10th century) to about 4.5 km during the Song dynasty (10th–13th century), and eventually to less than 500 m by the end of the Yuan dynasty (14th century) (Zhu, 1980b). The Song dynasty had conducted efforts to dredge and widen the lower Wusong River and its distributary, the palaeo-Qinglong channel,

including significant meander cut-off projects between Baoyuan (1038 CE) and Xuanhe (1119 CE) (Mao, 1990). However, these efforts failed to reverse the silting trend.

The ancient Qinglong Town, located west of modern-day Shanghai (Figures 1B, C), is the oldest known port town in the region. Strategically situated along the palaeo-Qinglong channel, it provided access to inland cities such as Suzhou and Huzhou to the west via the Wusong River, and Huating to the south via the Tongbotang waterway. However, rapid silting of the Qinglong channel during the Qiandao period (1165–1173 CE) of the Southern Song dynasty significantly reduced navigability. By the end of the 12th century, the channel was largely silted up, leading to a swift decline in trade activity at Port Qinglong (Zhang, 2007; Zou, 2007). Today, the Qinglong channel remains as a small watercourse about 10 m wide, still named as Port Qinglong (Figure 1C).

3 Materials and methods

In 2022, three cores (WSJ-1, WSJ-2, WSJ-3; Figure 1C) were drilled based on archaeological surveys and excavations of the ancient Port Qinglong, which determined the spatial distribution of the palaeo-Qinglong channel near the port town. WSJ-1 (121° 9'24.81"E, 31°15'22.40"N, 4.34 m above mean sea level) and WSJ-2 (121°9'27.34"E, 31°15'37.36"N, 4.03 m above mean sea level) were positioned within the palaeo-Qinglong channel, on the south and north banks of the present-day Port Qinglong, respectively. WSJ-3 (121°9'23.18"E, 31°16'30.26"N, 3.99 m above mean sea level) was drilled on the south bank of the present-day Wusong River, facilitating a comparative analysis to delineate the spatial extent and incision depth of the palaeo-Qinglong channel. Each core reached a depth of 20 m and was transported to the State Key Laboratory of Estuarine and Coastal Research (SKLEC) at East China Normal University (ECNU), where they underwent segmentation, description, photography, sampling, pretreatment, and measurement. The top soil of farmland in WSJ-1 and WSJ-2 and the modern artificial filling on the top of WSJ-3 were not sampled.

Five samples of plant debris and five OSL samples were collected from cultural layers and sedimentary sections with significant lithological changes in the three cores. A total of 169 samples, collected at 20 cm intervals, were analyzed for grain size and alkaline earth metals. AMS ^{14}C dating was performed by Beta Analytic, USA, and calibrated using the IntCal20 database in Calib 8.20 (Table 1). All other pretreatment and analyses were carried out at SKLEC.

OSL sample preparation and measurements were performed at the OSL Laboratory of SKLEC, with results presented in Table 2. Quartz grains (45–63 μm) were extracted following the procedures outlined by Nian et al. (2021, 2022). The single-aliquot regenerative-dose (SAR) protocol (Murray and Wintle, 2000) was used to determine the equivalent dose (D_e). A preheat temperature of 200° C for 10 s and a cut-heat of 160°C were employed, followed by 40 s of stimulation at 125°C. D_e values were derived from the initial 0.4 s of the decay curve, with late background subtraction based on the last 10 s, as the quartz signals from Holocene sediments in the area are

TABLE 1 AMS ^{14}C ages and their calibrations for cores WSJ-1, WSJ-2, and WSJ-3.

Core ID	Depth (m)	Materials	Conventional age (yr BP)	Calibrated age (cal. yr BP)			Lab No.
				2σ	Prob.	Median	
WSJ-1	6.32	Plant	1080 ± 30	928–1058	1	985	Beta-651150
WSJ-1	7.32	Plant	970 ± 30	792–928	1	855	Beta-651151
WSJ-1	13.82	Plant	7440 ± 30	8186–8340	1	8265	Beta-651152
WSJ-2	7.45	Plant	950 ± 30	788–922	1	850	Beta-661589
WSJ-2	16.28	Plant	7580 ± 30	8348–8418	1	8390	Beta-651154
WSJ-3	4.65	Plant	3760 ± 30	3989–4236	1	4120	Beta-651155

dominated by the fast component (Nian et al., 2019). Both the Central Age Model (CAM) and Minimum Age Model (MAM) (Galbraith et al., 1999) were used for age calculation, applying a sigma-b value of 0.1 for MAM calculations, following Nian et al. (2018a, 2018b). MAM ages were adopted for further discussion, as they yield robust D_e values for partially bleached sediments and align with CAM results for well-bleached samples (e.g., Wang et al., 2019). Luminescence measurements were performed on 2 mm aliquots mounted on 0.97 cm aluminum discs using Silkospray silicone oil. Given the low luminescence sensitivity and efficiency of quartz in the Holocene sediments of the Yangtze Delta, the application of small aliquots (2 mm) have been proved effective in identifying partial bleaching, thereby ensuring the reliability of the OSL age determinations (Nian et al., 2018b, 2021). The concentrations of U, Th, and K were measured using inductively coupled plasma mass spectrometry (ICP-MS).

Grain size analysis involved the following pretreatment steps. Samples (~0.2 g) were dried at a temperature below 40°C. A 10% hydrogen peroxide (H_2O_2) solution was added to remove organic matter. After soaking overnight, a 10% HCl solution was then added

to remove carbonates. The samples were rinsed with ultrapure water until the supernatants were neutral and subsequently analyzed using the LS13320 laser grain size analyzer (Coulter, USA).

For alkaline earth metal analysis, dried sediment samples were ground and passed through a 200-mesh sieve. A 0.2000 g subsample was reacted with 20 ml of 10% diluted acetic acid (HAc), stirred repeatedly, and allowed to settle overnight. The supernatant was collected and heated in a crucible to remove the acid. After evaporation, a 5‰ diluted nitric acid solution was added, and the concentrations of Sr, Ba, and Ca in the HAc-leachates were measured using an inductively coupled plasma optical emission spectrometer (ICP-OES, Thermo ICAP 7400, USA).

Furthermore, 18 surface sediment samples were collected from the floodplain and riverbed of the Huangpu River (Figure 1B) for alkaline earth metal analysis using the same HAc extracted method. To contextualize the results, Sr and Ba contents from 24 surface samples from the Yangtze River mouth and offshore areas (Wang et al., 2021) and seven from alluvial plains of the Taihu drainage basin (Zhang et al., 2022) were compiled for comparison with the core and surface sediments from this study.

TABLE 2 OSL ages for cores WSJ-1, WSJ-2, and WSJ-3 together with supporting data of dose rate and equivalent dose (D_e).

Core ID	Lab No.	Depth (m)	U (ppm)	Th (ppm)	K (%)	[a]Water content (%)	Grain size (μm)	Dose rate (Gy/ka)
WSJ-1	W2401	11.43	2.03 ± 0.10	11.68 ± 0.58	1.88 ± 0.09	25 ± 5	45–63	2.74 ± 0.12
WSJ-2	W2402	14.53	1.72 ± 0.09	10.26 ± 0.51	1.88 ± 0.09	24 ± 5	45–63	2.59 ± 0.11
WSJ-3	W2403	3.43	2.24 ± 0.11	11.99 ± 0.60	1.88 ± 0.09	26 ± 5	45–63	2.85 ± 0.12
WSJ-3	W2404	12.37	2.25 ± 0.11	13.64 ± 0.68	1.86 ± 0.09	28 ± 5	45–63	2.81 ± 0.12
WSJ-3	W2405	18.33	2.41 ± 0.12	15.10 ± 0.76	2.29 ± 0.11	27 ± 5	45–63	3.27 ± 0.12

Lab No.	Disc No.	OD (%)	[b]CAM D_e (Gy)	CAM Age (ka)	[b]MAM D_e (Gy)	MAM Age (ka)	Calibrated age (cal. yr BP)
W2401	28	30 ± 5	2.88 ± 0.18	1.05 ± 0.08	2.44 ± 0.12	0.89 ± 0.06	818 ± 60
W2402	21	16 ± 4	5.81 ± 0.25	2.24 ± 0.14	5.38 ± 0.36	2.08 ± 0.17	2008 ± 170
W2403	19	13 ± 3	11.60 ± 0.42	4.07 ± 0.23	11.60 ± 0.42	4.07 ± 0.23	3998 ± 230
W2404	21	36 ± 6	15.28 ± 1.24	5.43 ± 0.50	12.46 ± 0.57	4.43 ± 0.28	4358 ± 280
W2405	21	26 ± 4	21.67 ± 1.30	6.62 ± 0.49	15.57 ± 1.41	4.75 ± 0.46	4678 ± 480

All ages were calculated to values before 1950 CE to be consistent with the AMS ^{14}C age.
[a]Water content (%, defined as the ratio of water weight to dry sediment weight) was measured in the laboratory, with an assigned uncertainty of ±5%.
[b]The CAM and MAM represent the central age model and minimum age model, respectively.

4 Results

4.1 Lithology and chronology of the cores

Based on lithologies, sedimentary structures, and stratigraphic contacts, cores WSJ-1, WSJ-2, and WSJ-3 were divided into distinct stratigraphic units from bottom to top.

WSJ-1 was divided into four units. Unit A (20–17 m) consists of interbedded grey sand and mud (Figure 2A), sharply contacted with the overlying unit. Sand dominated with mud pebbles in the interval between 17.78–17 m. Unit B (17–13 m) is composed of homogeneous grey mud with numerous plants remains (Figure 2B), and occasional silt laminations at the base. Above 14 m, silt clumps are more frequent, with a sharp contact at the top. AMS ^{14}C dating at 13.82 m yielded a median age of 8265 cal. yr BP (Table 1). Unit C (13–1.0 m) is dominated by grey muddy silt with thin sand layers at the base (Figure 2C). Interbedded thin layers become prominent upward (Figure 2D), transitioning to yellowish-grey sediments with Fe/Mn oxides above 1.8 m (Figure 2F). Cultural layers were identified at 9.5–9.4 m, 8.45–8.0 m, and 7.3–6.03 m (Figure 2E), containing artefacts such as bricks, porcelain, shells, animal bones, and plant remains. The MAM OSL age at 11.43 m is

FIGURE 2
Photographs of typical lithological elements in cores WSJ-1 (A−F), WSJ-2 (G−L), and WSJ-3 (M−R). Note the various types of sand-mud couplets in each core.

818 ± 60 cal. yr BP (Table 2), while AMS ^{14}C dates at 7.32 m and 6.32 m are 855 and 985 cal. yr BP, respectively (Table 1). Unit D (above 1.0 m) consists of brownish-grey silty mud to yellow-brownish mud. Gastropod shells and pottery fragments occur in the lower part.

WSJ-2 was divided into three units. Unit A (20–16 m) comprises dark grey homogeneous mud with abundant plant debris (Figure 2G) and occasional silt laminae, sharply contacted with the overlying unit. Yellowish-grey mud nodules are common. The contact surface features a 20 cm thick layer of mud nodules (16–15.8 m) (Figure 2H). AMS ^{14}C dating at 16.28 m gives a median age of 8390 cal. yr BP (Table 1). Unit B (15.8–2.1 m) consists of thin interlayers of grey silty mud and muddy silt or fine sand (Figures 2I, J). Fine sand layers are prominent below 14 m, transitioning to mm-scale interlayers above 6 m (Figure 2K). The mud layers thicken gradually upward. The MAM OSL age at 14.53 m is 2008 ± 170 cal. yr BP (Table 2), and AMS ^{14}C dating at 7.45 m yields a median age of 850 cal. yr BP (Table 1). Unit C (2.16–0 m) transitions from brownish-grey to greyish-yellow silty mud upward, with abundant Fe/Mn oxides (Figure 2L).

WSJ-3 was divided into four units. Unit A (20.0–16.4 m) consists of grey silty mud with fine sand laminae (Figure 2M). Fine sand dominates the bottom. The MAM OSL age at 18.33 m is 4678 ± 480 cal. yr BP (Table 2). Unit B (16.4–11.56 m) is interbedded with silty mud and muddy silt, exhibiting high water content. The contact with the overlying unit is sharp. The MAM OSL dating at 12.37 m gives an age of 4358 ± 280 cal. yr BP (Table 2). Unit C (11.56–3.0 m)

contains thickly or thinly interbedded grey sand and mud. Sand layers (20–50 cm) dominate below 9.72 m, containing mud intraclasts and thin mud layers. Mud layers (2–6 cm thick) contain thin layers and laminae of sand. Shell fragments are common at erosional surfaces at the base of the sand layer (Figure 2N). Above 9.72 m, both sand and mud layers become thinner (Figure 2O). Plant debris is abundant in the mud layer at 4.65–4.20 m (Figure 2P), with AMS ^{14}C dating at 4.65 m gives a median age of 4120 cal. yr BP (Table 1). The MAM OSL age at 3.43 m is 3998 ± 230 cal. yr BP (Table 2). Unit D (3.0–1.14 m) consists of yellowish-grey silty mud with muddy silty sand laminae at 3.0–2.0 m. The sediments transition to yellowish-grey homogeneous mud with abundant Fe/Mn oxides above 2.0 m (Figure 2Q). Organic matter content increases between 1.7–1.45 m (Figure 2R). Above 1.14 m is modern artificial fill.

The MAM OSL and AMS ^{14}C ages were used to construct Bayesian age-depth models (Figure 3; Blaauw and Christen, 2011). Due to clear stratigraphic discontinuities, WSJ-1 was modeled up to 13 m and WSJ-2 up to 15.8 m where sharp contacts occur. The results demonstrate that the age-depth curve above 13 m in WSJ-1 is nearly vertical (Figure 3A), suggesting rapid deposition over a short period, with the most likely age range being 960–800 cal. yr BP and a median age of 868 cal. yr BP. For WSJ-2, the median age is approximately 2220 cal. yr BP at 15.8 m and 50 cal. yr BP at the top (Figure 3B). According to the limited dating results, the sedimentation rate is estimated at 0.61 cm/yr during 2220–850 cal. yr BP, increasing to 0.93 cm/yr since 850 cal. yr BP. The OSL
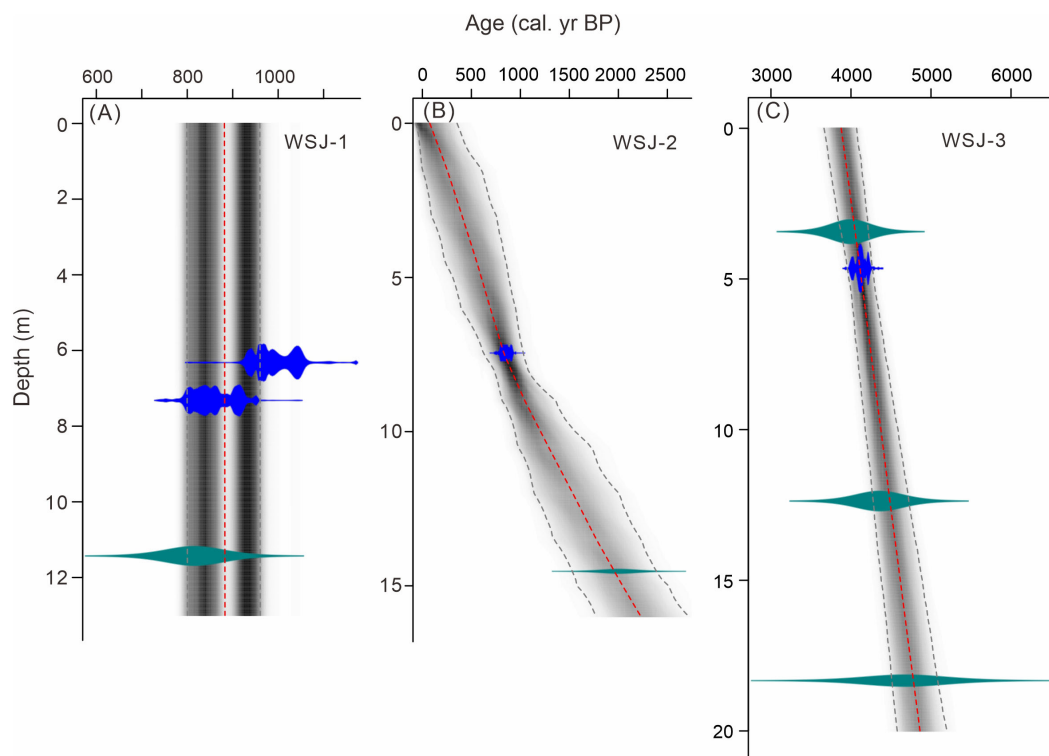

FIGURE 3
Bayesian age-depth models calculated according to the OSL (green) and AMS ^{14}C (blue) dating results for cores WSJ-1 **(A)**, WSJ-2 **(B)**, and WSJ-3 **(C)**.

and AMS ^{14}C ages from WSJ-3 form a consistent sequence (Figure 3C). The median age is 4860 cal. yr BP at the base and 3880 cal. yr BP at the top, with a nearly constant sedimentation rate of 2.04 cm/yr.

4.2 Vertical variations of grain size and alkaline earth metals

4.2.1 Core WSJ-1

Unit A (20.0–17.0 m) is the coarsest in the core, with an average sand content of 49% (Figure 4A). The median grain size is 32–115 μm, and the mean value is 64 μm. The mean grain size is also large, 32–131 μm, averaging 79 μm. Both unimodal and multimodal curves of the grain size frequency present, with peaks at 100–130 μm (Figure 5A). Sr and Ca contents and Sr/Ba ratio are the lowest in the core, with average values of 9.68 mg/kg, 0.84 mg/g and 0.45, respectively. In contrast, Ba content is relatively high, averaging 21.82 mg/kg (Figure 4A).

Unit B (17.0–13.0 m) are significantly finer than the previous unit, with clay and silt contents increase to 27% and 70%, respectively. The median grain size decreases to an average of 10 μm, the lowest value in the core. The mean grain size ranges from 11 to 29 μm, with an average value of 16 μm. The grain size frequency curve is broad and gentle, peaking near ~1 μm and 10 μm (Figure 5B). Sr, Ca contents and the Sr/Ba ratio increase significantly, averaging 24.89 mg/kg, 7.87 mg/g and 2.37 respectively. Ba content decreases to an average of 11.25 mg/kg.

Unit C (13.0–1.0 m) shows a decline in clay content (5–13%) and an increase in sand content (5–38%). Based on variations in grain size and contents of alkaline earth metals, the unit is further divided into three subunits C_1–C_3 (Figure 4A). The grain size frequency curve of C_1 (13.0–10.7 m) is unimodal, with a peak around 30 μm (Figure 5C). Sr and Ca contents, as well as the Sr/Ba ratio, increase further compared to Unit B, averaging 37.03 mg/kg, 17.91 mg/g and 4.26, respectively. Ba content decreases slightly to an average of 8.82 mg/kg. The grain size frequency curve of C_2 (10.7–4.4 m) is dominated by a single peak at ca. 30 μm or ca. 50 μm, with a secondary peak around 700 μm (Figure 5D). Sr and Ca contents increase significantly in cultural layers, reaching peak values of 95.47 mg/kg and 31.04 mg/g, consistent with the higher shell fragments content observed in the lithology. Ba content increases to 11.60–32.75 mg/kg, resulting in a lower Sr/Ba ratio compared to C_1. The grain size frequency curve of C_3 (4.4–1.0 m) narrows, with a steep unimodal peak at ca. 35 μm (Figure 5E). The contents of Sr, Ca and Ba and the Sr/Ba ratio are similar to C_1, averaging 32.56 mg/kg, 18.03mg/g, 8.57 mg/kg and 3.87, respectively.

Unit D (1.0–0.0 m) exhibits increased clay and silt contents, averaging 12% and 83%, respectively. The median and mean grain sizes are 24 μm and 27 μm, respectively. The grain size frequency curve is unimodal (Figure 5E, dotted line). Sr and Ca contents and the Sr/Ba ratio decrease significantly, while Ba content shows an increase.

4.2.2 Core WSJ-2

Unit A (20.0–16.0 m) is mainly composed of clay (22% on average) and silt (72% on average) (Figure 4B). The median grain size (11 μm on average) is the smallest across all units, and the mean grain size ranges from 11 μm to 32 μm (18 μm on average). The frequency curves of grain size are relatively broad and gentle, with a main peak at around 30 μm (Figure 5F). Elemental analysis shows low Sr and Ca contents and a low Sr/Ba ratio, with average values of 18.28 mg/kg, 7.79 mg/g and 1.20, respectively. Ba content is slightly elevated compared to other units, averaging 15.97 mg/kg.

Unit B (15.8–2.1 m) shows a marked increase in sand content. Based on variations in grain size and alkaline earth metals, it was subdivided into three subunits (B_1–B_3) (Figure 4B). B_1 (16.0–14.0 m) has the highest sand content in the core. The median and mean grain sizes are 49 μm and 18 μm on average, respectively. The grain size frequency curve is bimodal, with peaks at about 50 μm and 200 μm (Figure 5G). Sr and Ca contents increase significantly compared to Unit A, with averages of 23.93 mg/kg and 11.83 mg/g, respectively. Ba content decreases slightly to an average of 12.86 mg/kg, while the Sr/Ba ratio rises to 1.96. In B_2 (14.0–6.0 m), silt content increases significantly, while sand content decreases. Median and mean grain sizes drop to 32 μm and 70 μm, respectively. The grain size frequency curve is narrower, with a single peak primarily between 30 and 50 μm (Figure 5H). Sr, Ba, and Ca contents are similar to those in B_1, averaging 23.93 mg/kg, 11.83 mg/kg, and 14.78 mg/g, respectively. However, localized decreases in Ba content and abnormal increases in the Sr/Ba ratio are observed at certain depths. B_3 (6.0–2.1 m) shows an increase in clay content and a decrease in sand content. Median and mean grain sizes drop to 26 μm and 30 μm, respectively. The grain size frequency curve is unimodal, with a peak centered around 26 μm (Figure 5I). Sr and Ca contents are lower than in B_2, averaging 18.72 mg/kg and 11.27 mg/g. Ba content rises significantly but declines slightly in the upper part of the subunit, with an average of 17.39 mg/kg. The Sr/Ba ratio decreases markedly to an average of 1.16 (Figure 4B).

Unit C (2.1–0.0 m) gradually becomes finer upward, with clay and silt contents increasing to averages of 11% and 81%, respectively. Median and mean grain sizes are both 15 μm on average. The grain size frequency curve broadens but retains a unimodal shape, with a peak around 35 μm (Figure 5J). Sr and Ca contents are the lowest among all units, averaging 12.82 mg/kg and 5.82 mg/g. Ba content increases towards the top, averaging 19.06 mg/kg, while the Sr/Ba ratio is the lowest in the entire core, with an average of 0.67.

4.2.3 Core WSJ-3

Unit A (20.0–16.0 m) contains high sand content in the bottom 1 m (86%), with clay and silt contents increasing upward to 11% and 63%, respectively (Figure 4C). At the base, the median and mean grain sizes are 126 μm and 122 μm on average, decreasing upward to 38 μm and 48 μm. The grain size frequency curve exhibits a sharp single peak around 140 μm at the bottom, transitioning upward to double peaks with the main peak at ~30 μm (Figure 5K). Sr and Ca contents are the highest in the core, ranging from 24.68–51.18 mg/kg and 9.22–22.06 mg/g, respectively, but decrease upward. Ba content is relatively low, averaging 7.91 mg/kg. The Sr/Ba ratio is highest at the base (2.73 to 8.91) and decreases upward.
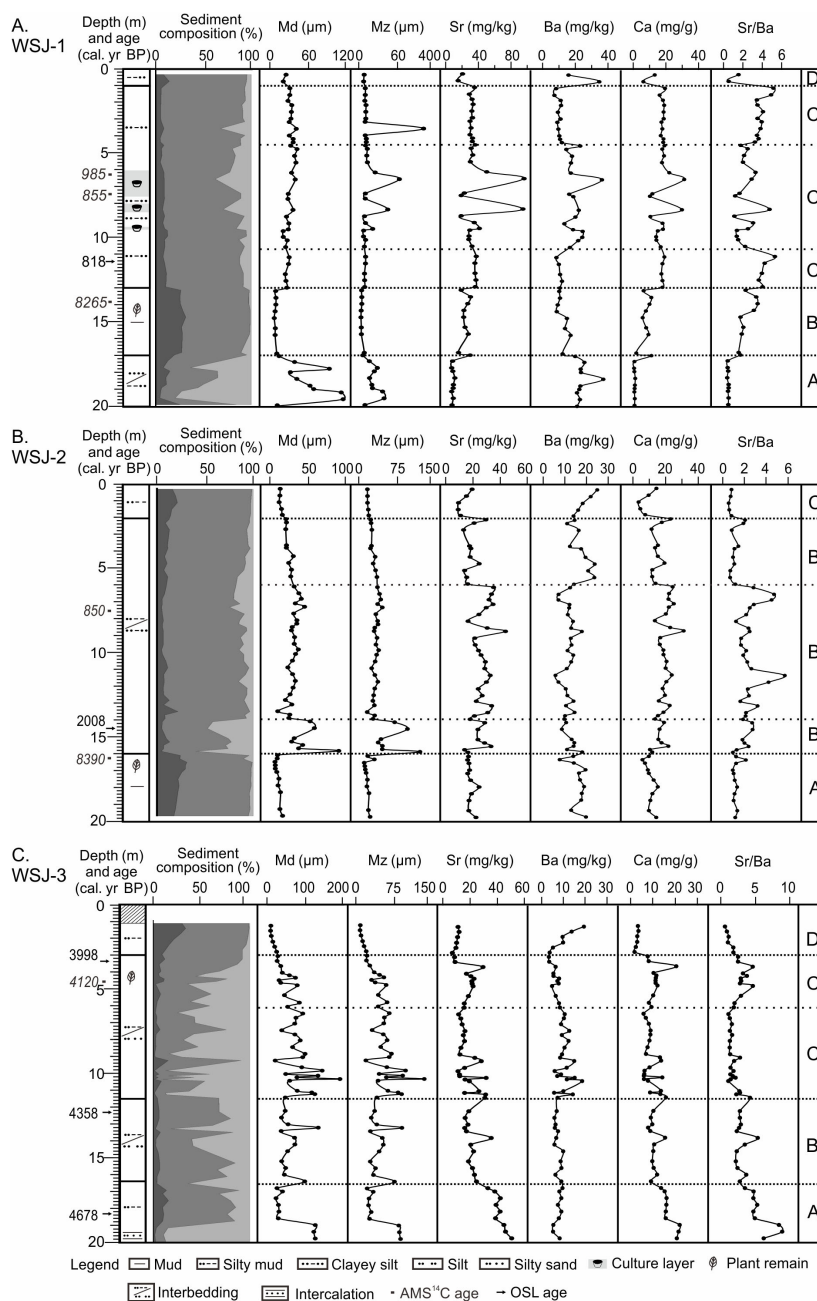
FIGURE 4
Composite depth profiles of cores WSJ-1 **(A)**, WSJ-2 **(B)**, and WSJ-3 **(C)**, showing the OSL and AMS ^{14}C ages, lithology, sediment composition, median (Md) and mean (Mz) grain sizes, concentrations of alkaline earth metals (Sr, Ba, and Ca), and Sr/Ba ratios in the HAc leachates.

Unit B (16.0–11.56 m) shows decreased clay content (6%) and increased sand content (38%). Median and mean grain sizes are 57 μm and 61 μm on average. The grain size frequency curve is predominantly single-peaked, with peaks between 30 and 100 μm (Figure 5I). Ba, Sr, and Ca contents, as well as the Sr/Ba ratio, are relatively low, averaging 7.22 mg/kg, 20.78 mg/kg, 10.41 mg/g, and 2.95, respectively.

Unit C (11.56–3.0 m) shows a significant increase in sand content, averaging 52%. Clay and silt contents average 6% and 42%, respectively. Based on fluctuations of grain size and alkaline earth metals, this unit is divided into two subunits (C$_1$ and C$_2$).

Median and mean grain sizes of subunit C$_1$ (11.56–6.2 m) are 87 μm and 91 μm on average, respectively. The grain size frequency curve is single-peaked, with the peak concentrated around 100–150 μm (Figure 5M). Ba content is relatively high, while Sr, Ca contents and the Sr/Ba ratio are low. C$_2$ (6.2–3.0 m) features finning upward, with fluctuating silt content. Median and mean grain sizes are 48 μm and 57 μm, respectively. The grain size frequency curve displays both single and double peaks, with peaks near 30 μm and 130 μm (Figure 5N). Sr and Ca contents slightly increase, Ba content decreases significantly, and the Sr/Ba ratio rises to 3.02.
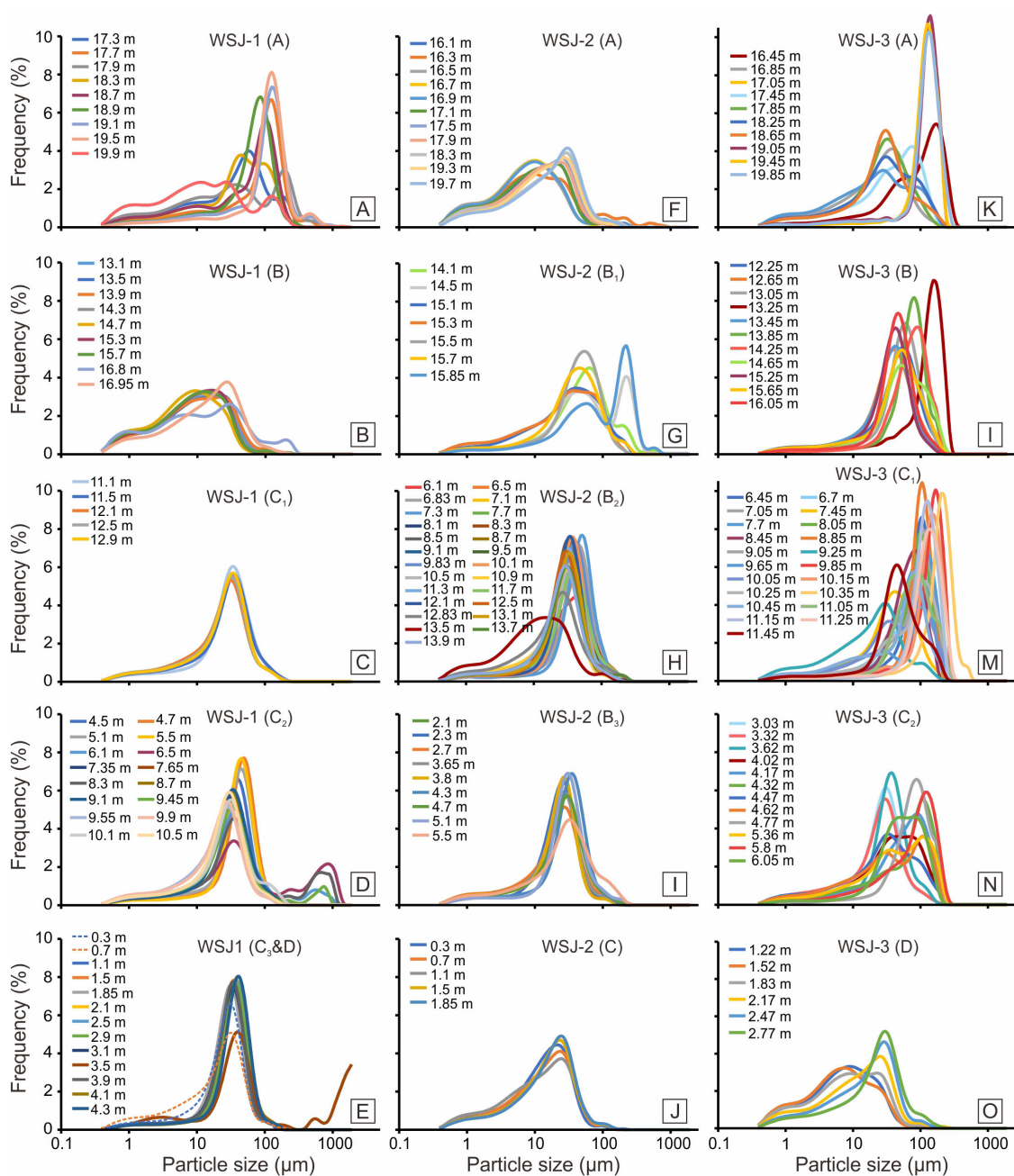
FIGURE 5
Grain size frequency curves of each unit and subunit for cores WSJ-1 **(A–E)**, WSJ-2 **(F–J)**, and WSJ-3 **(K–O)**. Unit and subunit divisions are consistent with Figure 4.

Unit D (3.0–0 m) exhibits finer sediments, with clay and silt contents increasing to 24% and 73% on average, respectively. Median and mean grain sizes decrease to 13 μm and 18 μm, respectively. The grain size frequency curve transitions from a single peak to a broader multi-peaked pattern, with the main peak shifting from ~28 μm at the bottom to ~8 μm at the top (Figure 5N). Sr and Ca contents are at their lowest levels in the core, averaging 9.72 mg/kg and 2.88 mg/g, respectively. Ba content increases significantly upwards, ranging from 6.53 to 19.43 mg/ kg, while the Sr/Ba ratio decreases to 1.71.

4.3 Comparison of alkaline earth metals in surface and core sediments

Surface sediments from the Huangpu River show significant differences in Ba and Sr contents between the middle and lower reaches (Figure 6A). Sediments in the middle reaches exhibit higher Ba and lower Sr contents, with median values of 41.23 mg/kg and 23.77 mg/kg and mean values of 48.69 mg/kg and 25.13 mg/kg. In contrast, sediments from the lower reaches showed a significant decrease in Ba content (median: 19.76 mg/kg, mean: 21.80 mg/kg),
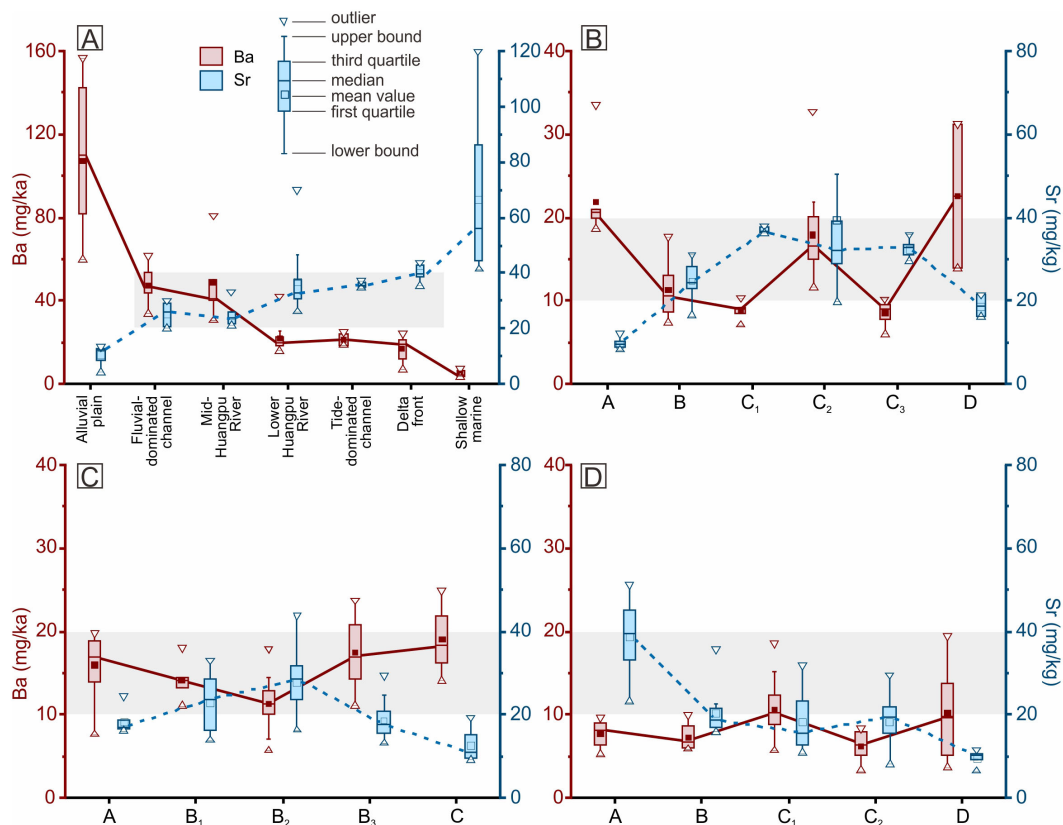
FIGURE 6
Box-and-whisker plots of Sr and Ba concentrations in surficial sediments collected from various sedimentary environment along the Yangtze coast and nearby shallow marine **(A)** and from core sediments of each unit and subunit in WSJ-1 **(B)**, WSJ-2 **(C)**, and WSJ-3 **(D)**. Data for alluvial plain sediments are from Zhang et al. (2022), and data for fluvial-dominated channel, tide-dominated channel, delta front, and shallow marine sediments are from Wang et al. (2021). The division of mid- and lower Huangpu River is indicated in Figure 1B. Shaded area indicates the major range of Sr concentration (20−40 mg/kg) in the fluvial to marine transition zone.

and an increase in Sr content (median: 32.66 mg/kg, mean: 37.14 mg/kg). The Sr/Ba ratio also differs, ranging from 0.41 to 0.69 in the middle reaches and increasing to 1.49–2.89 in the lower reaches.

Previous analyses of surface samples from the Yangtze coast revealed significant differences between terrestrial (e.g., alluvial plain of the Taihu drainage basin) and marine environments (Wang et al., 2021; Zhang et al., 2022). The middle and lower reaches of the Huangpu River and the Yangtze Delta show a consistent trend of decreasing Ba and increasing Sr from terrestrial to marine environments. Ba and Sr levels in the middle Huangpu River are distinct from terrestrial sources but align with fluvial-dominated, tidally influenced distributary channels of the Yangtze Delta. This suggests that the middle Huangpu River is a tidal river environment, receiving sediment input from both the Taihu drainage basin and the Yangtze Estuary. Conversely, the alkaline earth metal composition in the lower Huangpu River is similar to sediments from tide-dominated channels and the delta front of the Yangtze River mouth, indicating that a tide-dominated environment where sediments primarily originate from the Yangtze River mouth. The distance from Port Qinglong to the coastline during the Song dynasty is comparable to the length of the lower Huangpu River (Figure 1B). It is therefore speculated that Port Qinglong was located in a sensitive transition zone between tidal and fluvial dominance.

Ba content in the three cores is generally low (Figures 6B–D), aligning with samples from the lower Huangpu River, tide-dominated channels and the delta front of the Yangtze River mouth. Sr content shows wider variation. Units B and C in WSJ-1 and subunits B_1 and B_2 in WSJ-2 resemble sediments from the middle and lower Huangpu River and distributary channels of the Yangtze Delta. In particular, unit C in WSJ-1 and subunit B_2 in WSJ-2 are more similar to sediments from tide-dominated channels, while unit A in WSJ-3 is closer to the Yangtze Delta front. Conversely, Sr content in units A and D of WSJ-1, unit A, subunit B_3, and unit C in WSJ-2, as well as units B–D in WSJ-3, is generally lower than that in the distributary channels of the Yangtze Delta and the middle and lower Huangpu River, referring less influence from tides.

5 Discussion

5.1 Interpretation of sedimentary and hydrological environments at core sites

The evolution of sedimentary and hydrological environments at the three core sites was discussed based on lithological
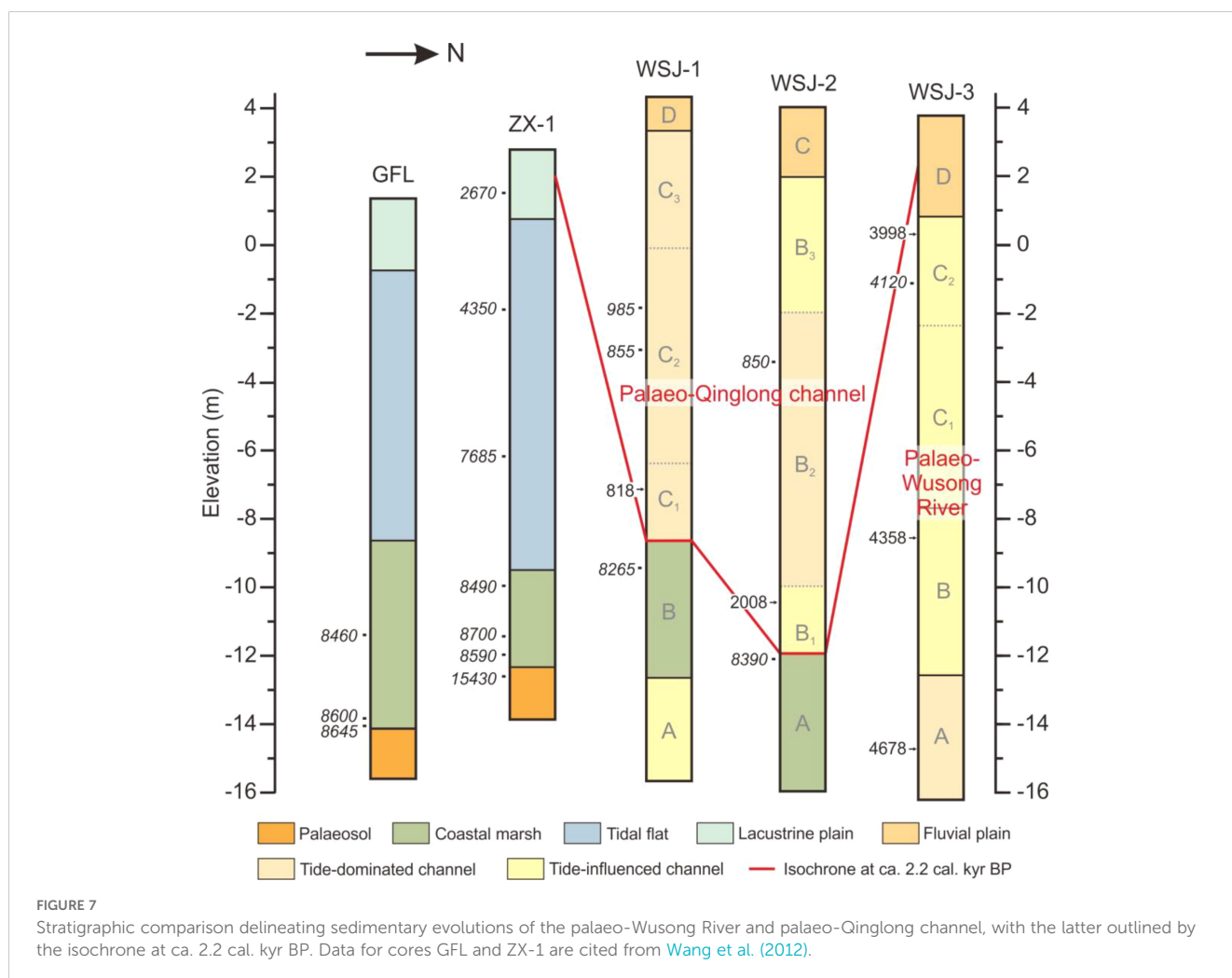
characteristics, grain size, and alkaline earth metal content, in conjunction with the dating results.

5.1.1 Core WSJ-1

The sand-mud interlayers with low Sr contents in unit A (Figures 2A, 4A) suggest deposition in a tidal river environment (Figure 7; Chen et al., 2015). The relatively low Ba content compared to the alluvial plain of the Taihu basin (Figure 6A), indicates that the sediments were primarily imported via tidal currents rather than fluvial discharge. In unit B, homogeneous mud enriched with plant debris (Figure 2B), coupled with increased Sr and decreased Ba contents (Figure 6B), suggests a shift towards a coastal marsh environment as marine influence increased. This aligns with previous research (Wang et al., 2013), which suggested a rapid rise in relative sea level in the southern Yangtze Delta from approximately −20 m to −15 m between 8.5 and 8.3 cal. kyr BP, followed by a slower rise and widespread development of tidal flats during 8.3–7.9 cal. kyr BP. This sea-level rise likely facilitated the transition from a tidal freshwater environment to a low-salinity coastal marsh. Adjacent cores, such as ZX-1 and GFL, also document the formation of coastal marshes on paleosols before 8.0 cal. kyr BP (Figure 7; Wang et al., 2012).

The stratigraphic discontinuity between units B and C (Figure 4A), combined with the chronology, suggests that unit C represents the palaeo-Qinglong channel (Figure 7). Increased Sr content and the proximity to the tide-dominated zone of the Yangtze River mouth (Figures 4A, 6B) indicate strong salinity intrusion. The unusually high Sr values in subunit C_2 may reflect anthropogenic influences, as these coincide with cultural layers. The increased sand content in this subunit, marked by a secondary grain size peak at 700 μm (Figure 5D), suggests enhanced fluvial processes, potentially associated with bedload transport during river floods (Chen et al., 2015). A concurrent increase in Ba content and a marked decrease in the Sr/Ba ratio in non-cultural layers (Figure 4A) support this interpretation. Historical literatures recorded numerous river regulation projects along the lower Wusong River, including the palaeo-Qinglong channel, during the 11th to early 12th centuries to improve freshwater drainage (Fu, 1998). This stratigraphic evidence likely corresponds to those activities. The finer sediments in subunit C_3 suggest weaker runoff-washing of the channel bed (Chen et al., 2015). Concurrently, a rising Sr/Ba ratio indicates renewed saltwater intrusion, which likely contributed to the rapid siltation of the Qinglong channel in the mid-to-late 12th century, as recorded in historical documents. Unit D, the uppermost 1-meter-thick layer, exhibits a significant increase in Ba content, likely representing post-siltation accumulation in the palaeo-Qinglong channel, transitioning into an alluvial plain environment influenced by tides.

FIGURE 7
Stratigraphic comparison delineating sedimentary evolutions of the palaeo-Wusong River and palaeo-Qinglong channel, with the latter outlined by the isochrone at ca. 2.2 cal. kyr BP. Data for cores GFL and ZX-1 are cited from Wang et al. (2012).

5.1.2 Core WSJ-2

The homogeneous mud rich in plant debris in unit A (Figure 2G), dated to ca. 8400 years ago, suggests deposition in a coastal marsh environment during the early Holocene, consistent with findings from cores WSJ-1, ZX-1, and GFL (Figure 7). Similar to WSJ-1, the sharp contact between units A and B, along with the dating results, indicates a substantial stratigraphic discontinuity, suggesting a transition to a channel environment at ca. 2.2 cal. kyr BP. The higher sand content in subunit B_1 (Figure 4B) indicates stronger hydrodynamic conditions, while the bimodal grain size frequency curves (Figure 5G) suggests contributions from both fluvial and tidal processes. Such deposition is analogous to that in the distributary channels of the Mekong Delta plain, where strong freshwater discharge during the flood season removes fine grains, leaving coarse bedload, while tidal processes dominate during the dry season, depositing fine sediments (Gugliotta et al., 2017; Ogston et al., 2017; Jiang et al., 2020). Alkaline earth metal contents and ratios indicate that tidal influence was stronger in unit B compared to unit A (Figure 6C).

The sudden increase in mud content in subunit B_2 reflects a significant import of mud by tidal currents and a concurrent weakening of fluvial processes (Chen et al., 2015). Although sand content increases towards the top of this subunit, it coincides with a decrease in Ba content and an increase in the Sr/Ba ratio (Figure 4B). The absence of a 200 μm peak in the grain size frequency curve, as seen in subunit B_1 (Figure 5H), suggests that the increased sand content is more likely due to intensified tidal currents, possibly linked to storm events. From subunit B_3 to unit C, the increasing mud content suggests a further weakening of hydrodynamic forces. However, the decrease in the Sr/Ba ratio indicates reduced saltwater intrusion, reflecting a transition to a freshwater tidal river and alluvial plain environment (Figures 6C, 7).

5.1.3 Core WSJ-3

The stratigraphy of WSJ-3 differs significantly from that of WSJ-1 and WSJ-2 (Figure 4C). With the exception of the top unit D, WSJ-3 is characterized by high sand content throughout, with grain size frequency peaks primarily at coarse grains (>100 μm; Figures 5K–M). This suggests a channel environment, likely corresponding to the channel bed of the palaeo-Wusong River. Chronostratigraphic data indicate that units A–C represent rapid deposition between 4.8 and 4.0 cal. kyr BP (Figure 3C), signifying the rapid siltation of the river channel and its subsequent transformation into an alluvial plain about 4000 years ago (Figure 7). Alkaline earth metal analyses reveal clear evidence of saltwater intrusion in unit A, while units B–D represent a transition to a tidally influenced freshwater or low-salinity environment (Figure 6D). Previous studies have documented the formation of chenier ridges east of the core sits around 7–4 cal. kyr BP, which largely blocked seawater intrusion into the Taihu Plain (Yan et al., 1989; Wang et al., 2012). The reduced saltwater influence observed in units B–D may reflect the protective effect of these chenier ridges.

In summary, after the palaeo-Wusong River silted up at the core site of WSJ-3 around 4000 years ago, the river likely changed course or developed new branches. The palaeo-Qinglong channel is speculated to have emerged as one such branch around 2000

years ago (Figure 7). However, the palaeo-Qinglong channel also silted up rapidly, as indicated by the chronology of unit C in WSJ-1. This siltation, along with salinity intrusion, primarily occurred during the 11th and 12th centuries (Figures 3A and 8A–C), corroborating historical accounts that the Qinglong channel was silted up by the end of the 12th century (Zhang, 2007). The lithology and fluctuations in alkaline earth metals in subunit B_2 of WSJ-2 are similar to those in unit C of WSJ-1 (Figures 4A, B). Combined with the dating results, it is suggested that subunit B_2 in WSJ-2 was also rapidly deposited during this period.

5.2 Mechanism and implications of the rapid siltation of the Qinglong channel

The salinity intrusion and rapid silting of the palaeo-Qinglong channel during the 11th and 12th centuries coincided with the MCA (9th to 13th centuries) in Europe (Figure 8). Previous studies suggest that eastern China experienced climate warming and an increase in typhoon events during the MCA (Figure 8D; Wang and Xie, 1999b; Xie and Yuan, 2012; Zheng et al., 2019; McKay et al., 2024). Additionally, an increase in relative sea level has been speculated during the Song dynasty, considered a response to this centennial-scale warming event (Man, 1988; Wang and Xie, 1999a; 1999b; 2001; Xie and Yuan, 2012; Man and Yang, 2014). Recent studies also reported that mid- to late Holocene warming periods were often accompanied by relative sea-level rise and/or increased storm surge frequency along the coast of Hangzhou Bay (Wang et al., 2018; Wu et al., 2022; Li et al., 2024). On a basin scale, rising sea levels increase the sediment accommodation capacity of river mouths, leading to enhanced sediment accumulation in estuaries and lower river reaches (Schumm, 1993). These factors provide the broader climatic and sea-level context for the siltation of the Qinglong channel.

The transition into a tide-dominated environment in the palaeo-Qinglong channel during the Song dynasty (Figure 7) further reveals changes in the hydro- and sediment dynamics of tide-dominated estuaries, driven by climate warming and rising sea levels. Tidal forces were significantly strengthened, while fluvial processes weakened at the mouth of the palaeo-Wusong River. We speculate that the enhanced tidal forces and associated rapid infilling in the palaeo-Qinglong channel were likely driven by the higher frequency of typhoons at that time (Table 3; Pan, 1995). Ge et al. (2020) observed that during storm surges in the Yangtze River mouth, the thickness of fluid mud in the maximum turbidity zone increased by up to 0.9 m, with storm tides also importing more fluid mud into the distributary channels. Without sufficient ebb tide flushing after the storm, this fluid mud would settle, contributing to rapid siltation. Meander cut-off projects downstream and upstream of Port Qinglong during the mid-11th to early 12th century (Man, 2007) may have temporarily enhanced freshwater discharge, but also reduced bottom friction for tide flows, thus facilitating mud import by flooding currents.

The reason for the weakening of fluvial processes during the Song dynasty is more complex. Droughts can be excluded because historical records widely document lake expansions and the
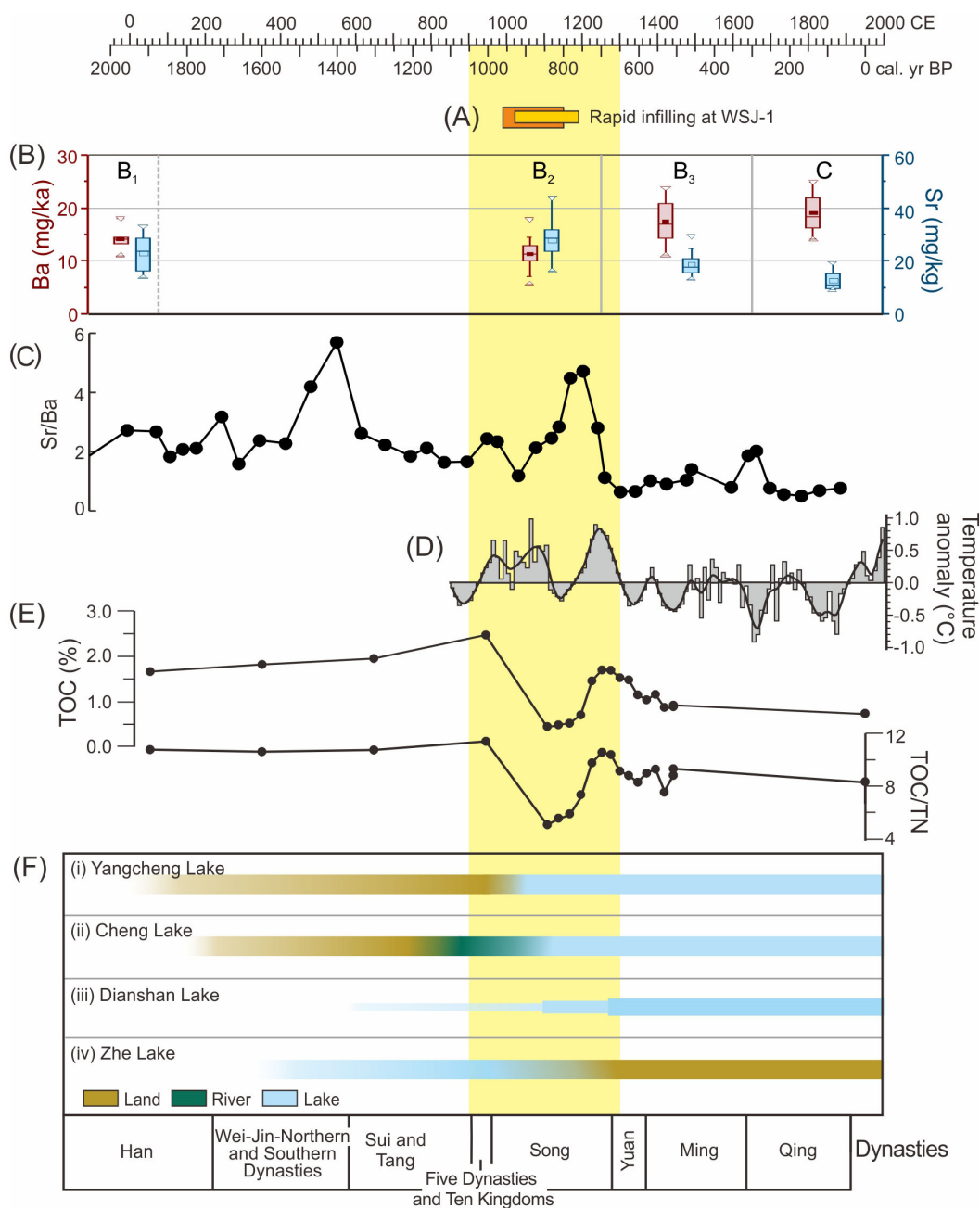
FIGURE 8

Comparison of the sedimentary records in the palaeo-Qinglong channel (A–C) with regional climate change (D) and lake evolution in the southern Yangtze Delta plain (E, F). (A) The rapid infilling during the 11–12th centuries as indicated by the chronology of core WSJ-1. The orange box refers to the age range calculated by the Bayesian age-depth model using all dating results (Figure 3A). The yellow box refers to the span between the oldest calibrated radiocarbon age (Table 1) and the youngest OSL age (Table 2). (B) Evidence of salinity intrusion during the 11–12th centuries based on increased Sr and declined Ba contents in subunit B_2 of core WSJ-2, potentially corresponding to unit C in WSJ-1. (C) Salinity intrusion during the 11–12th centuries indicated by the elevated Sr/Ba ratio recorded in core WSJ-2 based on the Bayesian age-depth model (Figure 3B). (D) Temperature anomaly changes in central and eastern China from the 9th century (after Hao et al., 2020). (E) Variations of TOC and TOC/TN in core DTX-4 (Chen et al., 2018), indicating the expansion of Luosheyang lake in the southwest delta plain. (F) The expansion of Yangcheng, Cheng, and Dianshan lakes in the central delta plain, and the infilling of Zhe Lake on the north bank of Hangzhou Bay. The period of Medieval Climatic Anomaly (MCA) is highlighted, corresponding largely to the Song dynasty in Chinese history, as shown at the bottom.

formation of new lakes at that time (Figures 8E, F). Some historical geographers argue that large-scale river regulation projects during the Tang and Song dynasties (e.g., the Songjiang Long Dike and the Wujiang Long Bridge), which reduced outflow from Taihu Lake and narrowed the upper Wusong River, were the main cause (Jing, 2022). However, we argue that runoff would have naturally deepened and adjusted the narrowed river channel. We propose that the low river gradient of the dish-like southern Yangtze Delta plain was the fundamental limiting factor. This depression was likely exacerbated during the Song dynasty by rising sea levels, as

TABLE 3 Historical records of storm events during the Song dynasty (Wen, 2006).

No.	Time	Historical storm event records
1	1st year of Yuanfeng, Northern Song (1078 CE)	In July, strong winds and heavy rain caused tides over 6.6 m, eroding embankments and bridges, leaving only stones behind.
2	8th year of Yuanyou, Northern Song (1093 CE)	Seawater overflowed, damaging farmland.
3	1st year of Shaosheng, Northern Song (1094 CE)	Seawater overflowed, damaging farmland.
4	28th year of Shaoxing, Southern Song (1158 CE)	In July, strong winds and heavy rain damaged farmland, causing famine.
5	1st year of Longxing, Southern Song (1163 CE)	In August, seawater overflowed, damaging farmland.
6	5th year of Shaoxi, Southern Song (1194 CE)	In July, seawater overflowed, damaging farmland.

The month referred to follows the lunar calendar.

the ground level near the shoreline would have needed to rise to keep pace with the increased tidal levels. This topography also facilitated waterlogging and lake expansion inland in the delta plain due to increased precipitation. Notably, Zhe Lake (Figure 1B) on the north bank of Hangzhou Bay reached its maximum extent during the late 10th and 11th centuries but rapidly silted up from tidal deposition and disappeared by the late 13th century (Sun, 2021). The rapid siltation of Zhe Lake parallels that of the palaeo-Qinglong channel, suggesting that rising sea levels and an increased frequency of storm events led to greater sediment input by tidal forces.

Rapid siltation of distributary channels around 700 years ago has also been reported in the tide-dominated Mekong Delta (Gugliotta et al., 2021). The infilling of the channel was characterized by the prevalence of muddy sediments, indicating tidal forces as the dominant sediment dynamic. It was speculated that this was induced by increased sediment supply due to climate change or human activities. Given its much larger freshwater discharge compared to the Wusong River, fluvial processes may have altered the bed morphology of the river channel and obstructed its entrance during extreme flood events. Subsequently, fluvial processes were largely reduced, and the distributary channel evolved into a tide-dominated environment.

In tide-dominated or influenced systems, whether driven by increased typhoon events or river floods blocking the channel entrance, the weakening of fluvial processes coupled with the strengthening of tidal forces can lead to rapid siltation. This is a critical characteristic of such systems. This phenomenon holds significant implications for global waterway management in tide-dominated river mouths, underscoring the need for more nuanced, region-specific approaches to estuarine and delta management.

6 Conclusions

This study examined sediments from three cores (WSJ-1, WSJ-2, and WSJ-3) near Qinglong Town, a prominent port during the Song dynasty, as well as surface sediments from the middle and lower reaches of the Huangpu River in Shanghai. By utilizing AMS

[14]C and OSL dating, along with grain size and alkaline earth metal measurements, the sedimentary and hydrological evolution of the lower Wusong River was reconstructed. The study also explored the dynamic processes driving the rapid siltation of the palaeo-Qinglong channel during the Song dynasty and the response of tidally influenced river channels to climate warming. The main conclusions are as follows:

1. The stratigraphy indicates that the Qinglong channel was formed about 2,000 years ago as a fluvial-dominated and tide-influenced system. During the Song dynasty (11th to 12th centuries), the channel experienced rapid siltation. Sedimentary records reveal significant saltwater intrusion, with deposition occurring primarily in a tide-dominated environment.
2. In WSJ-1, closest to Qinglong Town, evidence of bedload deposition was observed in the middle part of the sequence, formed in a tide-dominated environment during the Song dynasty. This suggests enhanced fluvial processes, potentially linked to river regulation projects recorded in historical documents from the 11th to early 12th centuries.
3. The rapid siltation of the palaeo-Qinglong channel was driven by relative sea-level rise associated with the MCA. This period saw a strengthening of marine forces, including tides and typhoons, which intensified the transport of marine-derived sediments to the lower Wusong River. The dish-like depression of the southern Yangtze Delta plain further limited the effectiveness of fluvial processes in clearing the riverbed, enabling the rapid accumulation of marine-derived sediments in the palaeo-Qinglong channel.

Data availability statement

The original contributions presented in the study are included in the article/supplementary material. Further inquiries can be directed to the corresponding authors.

Author contributions

Funding

Acknowledgments

Conflict of interest

The authors declare that the research was conducted in the absence of any commercial or financial relationships that could be construed as a potential conflict of interest.

Generative AI statement

The author(s) declare that no Generative AI was used in the creation of this manuscript.

Publisher's note

All claims expressed in this article are solely those of the authors and do not necessarily represent those of their affiliated organizations, or those of the publisher, the editors and the reviewers. Any product that may be evaluated in this article, or claim that may be made by its manufacturer, is not guaranteed or endorsed by the publisher.

References

Blaauw, M., and Christen, J. A. (2011). Flexible paleoclimate age-depth models using an autoregressive gamma process. *Bayesian Anal.* 6, 457–474. doi: 10.1214/ba/1339616472

Bradley, R. S., Hughes, M. K., and Diaz, H. F. (2003). Climate in medieval time. *Science* 302, 404–405. doi: 10.1126/science.1090372

Cai, R. S., and Tan, H. J. (2020). The impact and risks of accelerated sea level rise on low-elevation islands, coastal areas, and society. *Prog. Climate Change Res.* 16, 163–171. doi: 10.12006/j.issn.1673-1719.2019.225

Chen, T., Ryves, D. B., Wang, Z., Lewis, J. P., and Yu, X. (2018). Mid- to late Holocene geomorphological and hydrological changes in the south Taihu area of the Yangtze delta plain, China. *Palaeogeogr. Palaeoclimatol. Palaeoecol.* 498, 127–142. doi: 10.1016/j.palaeo.2018.03.012

Chen, S., Steel, R. J., and Olariu, C. (2015). "Chapter 7 - Palaeo-Orinoco (Pliocene) channels on the tide-dominated Morne L'Enfer delta lobes and estuaries, SW Trinidad," in *Fluvial-Tidal Sedimentology*, eds. P. J. Ashworth, J. L. Best and D. R. Parsons (Elsevier), 227–281. doi: 10.1016/B978-0-444-63529-7.00010-9.

Church, J., and White, N. (2011). Sea-level rise from the late 19th to the early 21st century. *Surveys Geophys.* 32, 585–602. doi: 10.1007/s10712-011-9119-1

Crowley, T. J., and Lowery, T. S. (2000). How warm was the medieval warm period? *AMBIO: A J. Hum. Environ.* 29, 51–54. doi: 10.1579/0044-7447-29.1.51

Fu, L. (1998). A new interpretation of the evolution of the lower reaches of Wusong River. *Acad. Monthly* 8, 89–94.

Galbraith, R. F., Roberts, R. G., Laslett, G. M., Yoshida, H., and Olley, J. M. (1999). Optical dating of single and multiple grains of quartz from Jinmium rock shelter, northern Australia: Part I, experimental design and statistical models. *Archaeometry* 41, 339–364. doi: 10.1111/j.1475-4754.1999.tb00987.x

Ge, J., Chen, C., Wang, Z. B., Ke, K., Yi, J., and Ding, P. (2020). Dynamic response of the fluid mud to a tropical storm. *J. Geophys. Res.: Oceans* 125, 1–27. doi: 10.1029/2019JC015419

Ge, Q., Liu, J., Fang, X., Yang, B., Hao, Z., Shao, X., et al. (2013). General characteristics of temperature change and centennial warm periods during the past 2000 years. *Acta Geogr. Sin.* 68, 579–592. doi: 10.11821/xb201305001

Gugliotta, M., Saito, Y., Nguyen, V. L., Ta, T. K. O., Nakashima, R., Tamura, T., et al. (2017). Process regime, salinity, morphological, and sedimentary trends along the fluvial to marine transition zone of the mixed-energy Mekong River delta, Vietnam. *Continental Shelf Res.* 147, 7–26. doi: 10.1016/j.csr.2017.03.001

Gugliotta, M., Saito, Y., Ta, T. K. O., Nguyen, V. L., La Croix, A. D., Wang, Z., et al. (2022). Late Holocene stratigraphic evolution and sedimentary facies of an active to abandoned tide-dominated distributary channel and its mouth bar. *Sedimentology* 69, 1151–1178. doi: 10.1111/sed.12940

Gugliotta, M., Saito, Y., Ta, T. K. O., Nguyen, V. L., Tamura, T., Wang, Z., et al. (2021). Abandonment and rapid infilling of a tide-dominated distributary channel at 0.7 ka in the Mekong River Delta. *Sci. Rep.* 11, 11040. doi: 10.1038/s41598-021-90268-6

Hao, Z., Wu, M., Liu, Y., Zhang, X., and Zheng, J. (2020). Multi-scale temperature variations and their regional differences in China during the Medieval Climate Anomaly. *J. Geogr. Sci.* 30, 119–130. doi: 10.1007/s11442-020-1718-7

Hay, C. C., Morrow, E., Kopp, R. E., and Mitrovica, J. X. (2015). Probabilistic reanalysis of twentieth-century sea-level rise. *Nature* 517, 481–484. doi: 10.1038/nature14093

Hong, X. (1991). Origin and evolution of Taihu Lake. *Mar. Geol. Quaternary Geol.* 4, 87–99. doi: 10.16562/j.cnki.0256-1492.1991.04.011

Hughes, M. K., and Diaz, H. F. (1994). Was there a "medieval warm period", and if so, where and when? *Clim. Change* 26, 109–142. doi: 10.1007/BF01092410

IPCC (2022). *Climate Change 2022: Impacts, Adaptation and Vulnerability. Working Group II Contribution to the IPCC Sixth Assessment Report.* Available online at: https://www.ipcc.ch/report/sixth-assessment-report-working-group-ii/.

Jiang, Y., Saito, Y., Ta, T. K. O., Wang, Z., Gugliotta, M., and Nguyen, V. L. (2020). Spatial and seasonal variability in grain size, magnetic susceptibility, and organic elemental geochemistry of channel-bed sediments from the Mekong Delta, Vietnam: Implications for hydro-sedimentary dynamic processes. *Mar. Geol.* 420, 106089. doi: 10.1016/j.margeo.2019.106089

Jing, C. (1985). The change of palaeogeographical environment of Tai Hu region during Holocene. *Geogr. Sci.* 3, 227–234.

Jing, M. (2022). The formation of upper watercourse of Wusong River during Tang and Song dynasties. *J. Chin. Historical Geogr.* 37, 16–24.

Jing, M. (2023). Southeast water flow out of the Taihu Lake and expansion of Dianshan Lake in the Song and Yuan dynasties. *Chin. Historical Geogr.* 43, 20–33.

Lamb, H. H. (1965). The early medieval warm epoch and its sequel. *Palaeogeogr. Palaeoclimatol. Palaeoecol.* 1, 13–37. doi: 10.1016/0031-0182(65)90004-0

Li, X., You, X., Lin, S., Zhang, W., Cheng, Z., and Wang, Z. (2024). Late holocene climate warming events and their linkage to hydraulic engineering on the coast of Hangzhou Bay, East China. *J. Mar. Sci. Eng.* 12, 79. doi: 10.3390/jmse12010079

Man, Z. (1988). Sea level rise during the Song dynasty and its environmental impacts. *J. Catastrophol.* 2, 71–78.

Man, Z. (2007). Evolution of the river channel around Baihehui and Panlonghui of Wusong River in Song Dynasty. *Historical Geogr.* 22, 343–351.

Man, Z., and Yang, Y. (2014). The medieval warming Impacts on the natural environment in eastern China as inferred from historical documents. *Quaternary Sci.* 34, 1197–1203. doi: 10.3969/j.issn.1001-7410.2014.06.08

Mao, B. (1990). *History of Shanghai Port* (Beijing: China Communication Press).

McKay, N. P., Kaufman, D. S., Arcusa, S. H., Kolus, H. R., Edge, D. C., Erb, M. P., et al. (2024). The 4.2 ka event is not remarkable in the context of Holocene climate variability. *Nat. Commun.* 15, 6555. doi: 10.1038/s41467-024-50886-w

Murray, A. S., and Wintle, A. G. (2000). Luminescence dating of quartz using an improved single-aliquot regenerative-dose protocol. *Radiat. Meas.* 32, 57–73. doi: 10.1016/S1350-4487(99)00253-X

Ni, H., and Ji, L. (1997). Environmental changes and formation of Yangcheng Lake area from ancient cultural sites. *J. Lake Sci.* 9, 35–40.

Nian, X., Zhang, W., Qiu, F., Qin, J., Wang, Z., Sun, Q., et al. (2019). Luminescence characteristics of quartz from Holocene delta deposits of the Yangtze River and their provenance implications. *Quaternary Geochronol.* 49, 131–137. doi: 10.1016/j.quageo.2018.04.010

Nian, X., Zhang, W., Wang, X., Hutchinson, S. M., Zhao, X., and Liu, K. (2022). Multi-centennial variability of Yangtze Delta growth over the last 2000 years: interplay of climate and people. *Earth's Future* 10, e2021EF002461. doi: 10.1029/2021EF002461

Nian, X., Zhang, W., Wang, Z., Sun, Q., and Chen, Z. (2021). Inter-comparison of optically stimulated luminescence (OSL) ages between different fractions of Holocene deposits from the Yangtze delta and its environmental implications. *Mar. Geol.* 432, 106401. doi: 10.1016/j.margeo.2020.106401

Nian, X., Zhang, W., Wang, Z., Sun, Q., Chen, J., and Chen, Z. (2018a). Optical dating of Holocene sediments from the Yangtze River (Changjiang) Delta, China. *Quaternary Int.* 467, 251–263. doi: 10.1016/j.quaint.2018.01.011

Nian, X., Zhang, W., Wang, Z., Sun, Q., Chen, J., Chen, Z., et al. (2018b). The chronology of a sediment core from incised valley of the Yangtze River delta: Comparative OSL and AMS ^{14}C dating. *Mar. Geol.* 395, 320–330. doi: 10.1016/j.margeo.2017.11.008

Ogston, A. S., Allison, M. A., Mullarney, J. C., and Nittrouer, C. A. (2017). Sediment- and hydro-dynamics of the Mekong Delta: From tidal river to continental shelf. *Continental Shelf Res.* 147, 1–6. doi: 10.1016/j.csr.2017.08.022

Pan, F. (1995). On the huge windstorm tide during historical times in the coastal areas of Jiangsu and Zhejiang province. *J. Nanjing Normal Univ. (Natural Sci. Edition)* 18, 94–101.

Plater, A., Long, A., Spencer, C., and Delacour, R. (1999). The stratigraphic record of sea-level change and storms during the last 2000 years: Romney Marsh, southeast England. *Quaternary Int.* 55, 17–27. doi: 10.1016/S1040-6182(98)00020-2

Qiao, S. (1980). The rise and fall of Qinglong Town and the rise of Shanghai. *Historical Geogr.* 6, 331–334.

Schumm, S. A. (1993). River response to baselevel change: implications for sequence stratigraphy. *J. Geol.* 101, 279–294. doi: 10.1086/648221

Shi, K., Dai, X., Shi, Y., and Yu, L. (2009). Grain-size characteristics and their paleoenvironmental significance of SC7 core sediments in Lake Chenghu, Jiangsu Province, China. *J. Lake Sci.* 21, 741–748. doi: 10.3321/j.issn:1003-5427.2009.05.020

Sun, C. (2021). Textural research on Zhehu Lake in Jinshan District of Shanghai. *Shanghai Chronicles* 2, 58–64.

Wang, H. (2016). A new series of the local annals of Qinglong Town. *Cultural Heritage Cities* 4, 109–159.

Wang, A., Wang, Z., Liu, J., Xu, N., and Li, H. (2021). The Sr/Ba ratio response to salinity in clastic sediments of the Yangtze River Delta. *Chem. Geol.* 559, 119923. doi: 10.1016/j.chemgeo.2020.119923

Wang, W., and Xie, Z. (1999a). Historical sea level fluctuations in China (II) tidal disaster intensity and sea level change. *J. Hohai Univ. (Natural Sciences)*, 43–47. doi: 10.3321/j.issn:1000-1980.1999.05.009

Wang, W., and Xie, Z. (1999b). Historical sea level fluctuations in China (I)-seawall engineering and sea level change. *J. Hohai Univ. (Natural Sciences)*, 7–11. doi: 10.3321/j.issn:1000-1980.1999.04.002

Wang, W., and Xie, Z. (2001). Preliminary approach to sea-level change in China basing Chinese historical documents. *Adv. Earth Sci.*, 272–278. doi: 10.3321/j.issn:1001-8166.2001.02.021

Wang, Z., Zhan, Q., Long, H., Saito, Y., Gao, X., Wu, X., et al. (2013). Early to mid-Holocene rapid sea-level rise and coastal response on the southern Yangtze delta plain, China. *J. Quaternary Sci.* 28, 659–672. doi: 10.1002/jqs.2662

Wang, F., Zhang, W., Nian, X., Ge, C., Zhao, X., Cheng, Q., et al. (2019). Refining the late-Holocene coastline and delta development of the northern Yangtze River delta: Combining historical archives and OSL dating. *Holocene* 29, 1439–1449. doi: 10.1177/0959683619854522

Wang, Z., Zhuang, C., Saito, Y., Chen, J., Zhan, Q., and Wang, X. (2012). Early mid-Holocene sea-level change and coastal environmental response on the southern Yangtze delta plain, China: implications for the rise of Neolithic culture. *Quaternary Sci. Rev.* 35, 51–62. doi: 10.1016/j.quascirev.2012.01.005

Wang, Z., Saito, Y., Zhan, Q., Nian, X., Pan, D., Wang, L., et al. (2018). Three-dimensional evolution of the Yangtze River mouth, China during the Holocene: impacts of sea level, climate and human activity. *Earth-Science Reviews* 185, 938–955. doi: 10.1016/j.earscirev.2018.08.012

Wei, S. (1979). The historical changes of the Taihu Lake water system. *Fudan J. (Social Sci. Edition)* 2, 58–64.

Wen, K. (2006). *China Meteorological Disasters Encyclopedia* (Beijing, China: Meteorological Press).

Williams, S. J. (2013). Sea-level rise and coastal change: Causes and implications for the future of coasts and low-lying regions. *J. Coast. Res.*, 184–196. doi: 10.2112/SI63-015.1

Wu, Y., Huang, X., Zheng, X., Meadows, M. E., and Wang, Z. (2022). Sedimentary records of mid-Holocene extreme storm events on the north bank of Hangzhou Bay, East China. *Mar. Geol.* 451, 106891. doi: 10.1016/j.margeo.2022.106891

Xie, Z., and Yuan, L. (2012). Fluctuation characteristics of Holocene sea-level change and its environmental implications. *Quaternary Sci.* 32, 1065–1077. doi: 10.3969/j.issn1001-7410.2012.06.02

Xu, Q. (1997). *Shanghai Water Resources Chronicle* (Shanghai, China: Shanghai Social Sciences Press).

Yan, Q., Xu, S., and Shao, X. (1989). Holocene cheniers in the Yangtze Delta, China. *Mar. Geol.* 90, 337–343. doi: 10.1016/0025-3227(89)90135-7

Zhang, X. (2006). *Studies on historical geomorphology and ancient maps of China* (Beijing: Social Science Literature Publishing House).

Zhang, X. (2007). Historical process of the evolution of the Qinglong River. *Historical Geogr.* 22, 335–342. (In Chinese)

Zhang, J. (2019). Reasons for the decline of Qinglong Town during the Song and Yuan dynasties. *J. Soc. Sci.* 3, 136–148.

Zhang, W., Zheng, T., Wang, Z., and Meadows, M. E. (2022). Reconstruction of coastal flooding processes and human response at the end of the Liangzhu Culture, East China. *Quaternary Sci. Rev.*, 509–517. doi: 10.1016/j.quascirev.2022.107705

Zheng, J., Liu, Y., Wu, M., Zhang, X., and Hao, Z. (2019). Evidences and regional differences on multi-scales in Medieval Climate Anomaly over China. *Acta Geogr. Sin.* 74, 1281–1291. doi: 10.11821/dlxb201907001

Zhu, K. (1973). A preliminary study of climate change in China over the past 5,000 years. *Sci. China* 02, 168–189.

Zhu, S. (1980a). The changes of the main water systems in the Taihu Basin during historical times. *Fudan J. (Social Sci. Edition)* S1, 43–52.

Zhu, S. (1980b). The historical evolution of the Wusong Jiang (River). *J. East China Normal Univ. (Natural Sci. Editon)* 02, 102–111.

Zou, Y. (2007). The rise and fall of Qinglong Town. *Historical Geogr.* 22, 331–334.